Journal of Geophysical Research: Solid Earth

RESEARCH ARTICLE
10.1029/2018JB016058

Friction of Mineralogically Controlled Serpentinites and Implications for Fault Weakness

T. Tesei[1], C. W. A. Harbord[1], N. De Paola[1], C. Collettini[2], and C. Viti[3]

[1]Department of Earth Sciences, Durham University, Durham, UK, [2]Dipartimento di Scienze della Terra, Università La Sapienza di Roma, Roma, Italy, [3]Università degli Studi di Siena, Roma, Italy

Key Points:
- We characterized the friction of serpentine serpentine samples that were carefully characterized from the mineralogical point of view
- Friction of lizardite and fibrous serpentines is low up to elevated temperature (T = 170°C)
- The friction of lizardite and fibrous serpentines accounts for the observed weakness of several major faults

Supporting Information:
- Supporting Information S1

Correspondence to:
T. Tesei,
telemaco.tesei@durham.ac.uk

Citation:
Tesei, T., Harbord, C. W. A., De Paola, N., Collettini, C., & Viti, C. (2018). Friction of mineralogically controlled serpentinites and implications for fault weakness. *Journal of Geophysical Research: Solid Earth*, *123*, 6976–6991. https://doi.org/10.1029/2018JB016058

Received 3 MAY 2018
Accepted 12 JUL 2018
Accepted article online 19 JUL 2018
Published online 15 AUG 2018

Abstract Serpentines are common minerals in several major tectonic faults in a variety of geodynamic settings and have variable frictional strength and complex deformation processes. Here we present friction experiments carried out on a suite of serpentine samples that include veins of antigorite, lizardite, and fibrous serpentine (chrysotile and polygonal serpentine) together with massive samples of retrograde (lizardite and chrysotile rich) and prograde (antigorite-rich) serpentinites. These samples were characterized from the hand specimen down to the nanoscale to precisely constrain their mineralogical composition and are interpreted to represent typical fault rocks and host rocks in serpentine-bearing shear zones, respectively. Experiments were performed at effective normal stress from 5 to 120 MPa, at temperatures of 25°C and 170°C and water-saturated, that is, under the faulting conditions of the brittle upper lithosphere. Friction of antigorite samples, either massive or vein, is relatively high $\mu = 0.53$. Retrograde, massive serpentinites, constituted primarily of lizardite and fibrous serpentines, are frictionally weak, $\mu = 0.30$. End-members lizardite and fibrous serpentines are even weaker, $0.15 < \mu < 0.19$, and this weakness is unchanged at high temperature. We document deformation of lizardite and fibrous serpentines occurring predominantly via mode II cracking, crystal/fiber folding, and frictional sliding, which account for the observed mechanical weakness. When combined with frictional reactivation analysis, our data provide mechanical evidence for fault weakness inferred from earthquake dip distributions at oceanic outer rises and low-angle normal faults beneath rifted continental margins and at slow/ultraslow spreading mid-ocean ridges.

1. Introduction

Serpentines are abundant minerals that Bailey et al., 2000; form by hydration processes of mafic and ultramafic rocks. Serpentinization is associated with major fault zones that provide pathways for seawater leading to the hydrothermal alteration of mantle rocks (e.g., Deschamps et al., 2013; Guillot et al., 2015, for extensive reviews). The main serpentine minerals are antigorite (corrugated structure), lizardite (platy), and chrysotile (fibrous) together with a range of intermediate structures such as polygonal and polyhedral serpentine. P-T conditions, reaction kinetics, and deformation control serpentine assemblage in rocks (Andréani et al., 2005; Evans, 2004). In general, lizardite, chrysotile and intermediate serpentines, such as polygonal serpentine, are stable under upper crustal conditions ($T < 400$°C, e.g., Andréani et al., 2007; Evans, 2004). In particular, they mostly form in ultramafic rocks altered under greenschist retrograde conditions ("retrograde serpentines" hereinafter). Conversely, antigorite is stable at higher temperature (~350–600°C) and plays a role in deep deformation processes (e.g., Schwartz et al., 2013). Serpentines are abundant rock-forming minerals in transform faults (e.g., Irwin & Barnes, 1975; Mével, 2003, and references therein) and at slow- and ultraslow-spreading mid-ocean ridges and ocean-continent transition, typically associated to detachment faulting in mantle rocks (e.g., Beslier et al., 1996; Boschi et al., 2006; Karson et al., 2006; Manatschal et al., 2011; Sauter et al., 2013). Serpentine-rich rocks are also widespread along normal faults that form by bending of oceanic plates entering subduction zones (e.g., Grevemeyer et al., 2018) and in ophiolitic units in orogenic belts (e.g., Coleman, 1971; Deschamps et al., 2013, and references therein).

The abundance and intimate association of serpentinites with major fault zones motivated a large number of studies on their mechanical properties. At elevated pressure ($P >$ 200–300 MPa) and/or temperature ($T > 300$°C) intact serpentinites show low fracture strength with respect to quartzo-feldspathic rocks, and unaltered mafic/ultramafic rocks (e.g., Amiguet et al., 2012; Escartin et al., 1997, 2001; Raleigh & Paterson, 1965, and references therein). The frictional properties of serpentine gouges, which control the strength and other mechanical properties of tectonic faults, are complex. At *P-T* conditions relevant for brittle faulting and seismogenesis, the frictional strength (ratio of shear to normal stress, μ) of the serpentines shows a broad range of

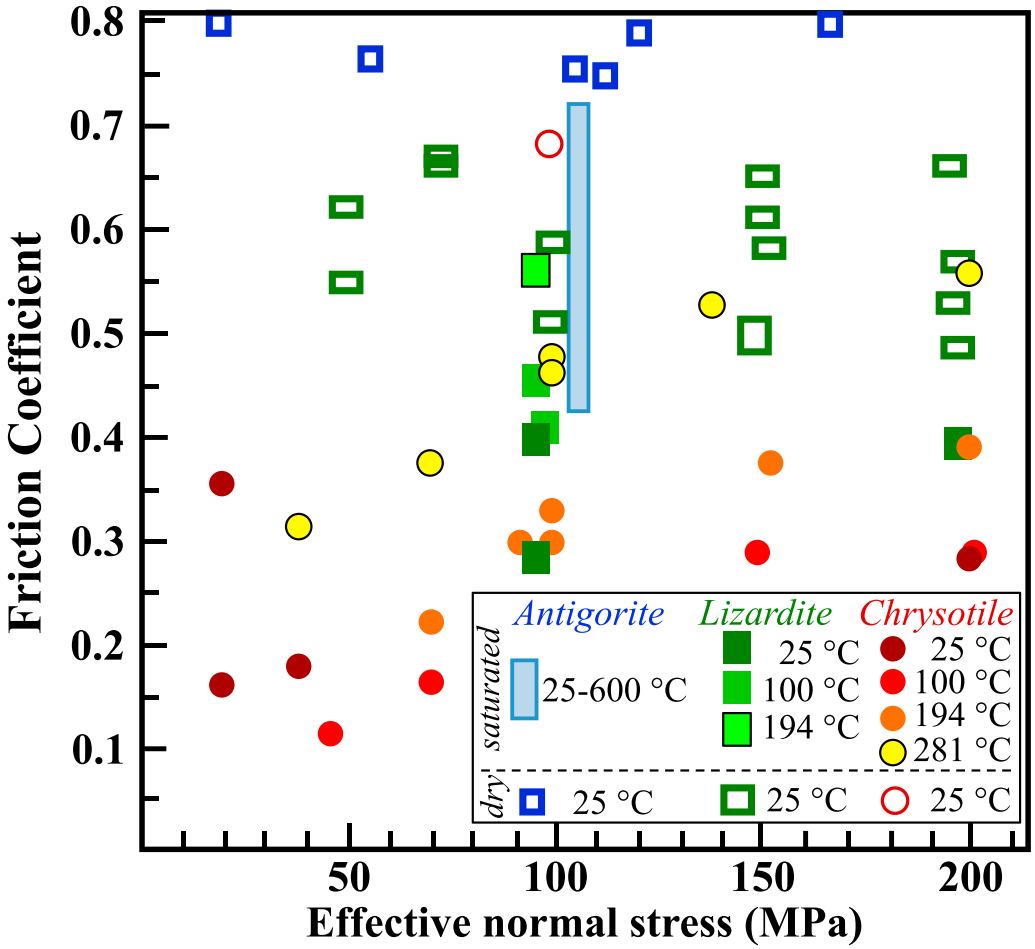

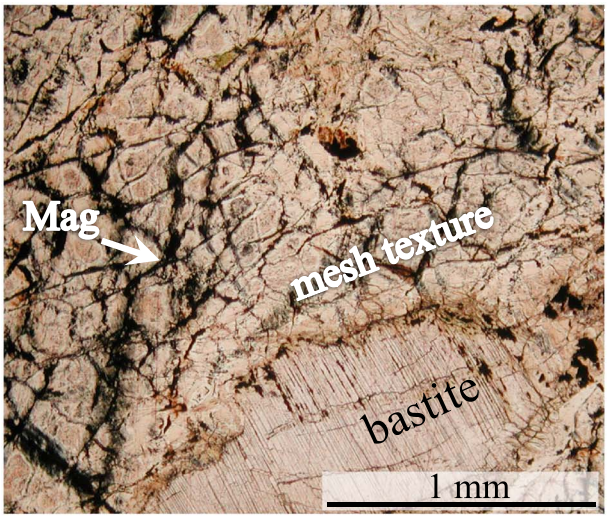

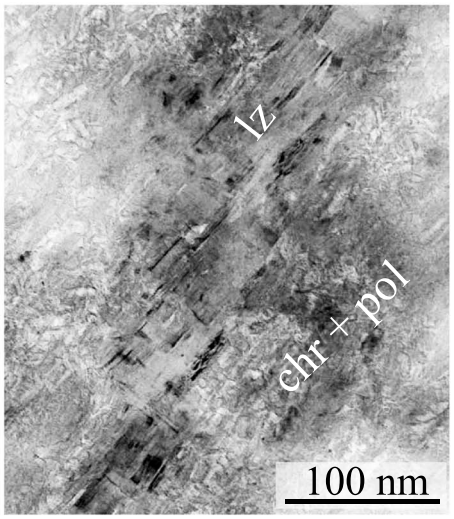

Figure 1. (a) Compilation of friction coefficient versus effective normal stress (normal stress or confining pressure – internal fluid pressure) for the three main varieties of serpentine minerals from the literature. Lizardite data (green squares) were compiled from Moore et al. (1997) and references therein and from Behnsen and Faulkner (2012). Chrysotile data (circles) were compiled from Moore et al. (2004). Antigorite data (blue squares) are compiled from Dengo and Logan (1981, dry bare surfaces) and from Takahashi et al. (2011, saturated gouges). (b) Textural complexity of a typical massive retrograde serpentinite. Mesh texture characterized by serpentine (lizardite and fibrous serpentines) rimmed by magnetite grains, derived from serpentinization of olivine, and a bastite (pseudomorphic replacement of pyroxene with serpentine). (c) Detail of a mesh core highlighting the nanoscale mixture of different serpentine varieties (lizardite, chrysotile, and polygonal serpentine).

values (Figure 1a). The friction of antigorite is reported to be relatively high, μ = 0.50–0.75 (Moore et al., 1997; Takahashi et al., 2011), similar to the average friction of rocks (μ = 0.60–0.85, Byerlee, 1978). The friction coefficient of saturated lizardite gouges is reported to vary between μ = 0.29–0.56 (Behnsen & Faulkner, 2012; Moore et al., 1997; Moore & Lockner, 2011) and the strength of saturated chrysotile between μ = 0.1–0.55 (Moore et al., 1997, 2004). The frictional strength of water-saturated gouges of both lizardite and chrysotile is reported to significantly increase at temperatures above 100°C, approaching their dry strength (μ = 0.6–0.7), potentially because of water desorption from mineral surfaces (Moore et al., 1997; Summers & Byerlee, 1977; Figure 1a).

Such variability of friction values is possibly due to the fact that serpentine minerals are extremely complex to study in laboratory experiments. Serpentines are often intermingled with abundant secondary minerals (e.g., Figure 1b) and are characterized by generally small crystal sizes and complex textures (e.g., Wicks & Whittaker, 1977). With the possible exception of some monomineralic chrysotile veins, the different serpentine polymorphs are difficult to separate for mechanical study, as they typically form ultrafine mixtures of small crystals (few micrometers or less, e.g., Figure 1c). These characteristics make the identification of the different serpentines species and their relative abundance in a rock challenging, particularly using routine analytical techniques such as optical microscopy (OM) and X-ray diffraction. Conversely, transmission electron microscopy (TEM) provides unambiguous, albeit spatially limited, identification of serpentine mineralogy (e.g., Viti & Mellini, 1998).

To contribute to the characterization of the friction of serpentine minerals, we combined several analytical techniques, including TEM, to characterize the mineralogical composition and microstructure of a suite of serpentines samples, down to the nanoscale. We selected samples of end-member serpentines of antigorite, lizardite, and fibrous serpentines (chrysotile and polygonal serpentine) from veins and massive samples of retrograde and prograde serpentinites. We then performed friction experiments to test the strength of these samples across a range of *P-T* conditions, relevant to the brittle faulting in the upper lithosphere.

2. Selection and Characterization of Serpentine Samples

We selected serpentine samples from a Ligurian ophiolite cropping out in the Elba Island (Central Italy, Bortolotti et al., 2007; Keller & Pialli, 1990; see supporting information). The mineralogy of these samples was accurately investigated by optical microscopy, XRD, scanning electron microscopy (SEM), TEM, and selected area electron diffraction, electron microprobe, thermal analyses, and spectrometric techniques (e.g., Mellini & Viti, 1994; Viti & Hirose, 2010; Viti & Mellini, 1996, 1998; this study).

We selected samples of (1) a massive retrograde serpentinite, (2) highly crystalline lizardite veins, (3) slickenfiber veins of fibrous serpentines (chrysotile and polygonal serpentine), (4) slickenfiber veins of antigorite, and (5) massive prograde antigorite serpentinite.

The selected samples represent all the main end-members of the serpentine group, that is, the vein samples characterized by remarkably uniform mineralogy, and serpentinitic rocks characterized by massive structure and the presence of secondary phases. Figure 2 summarizes the typical microstructure and mineralogical characteristics of the samples subsequently used in friction experiments (see supporting information for further details).

Undeformed, retrograde massive serpentinites (Figures 2a and 2b) are characterized by mesh textures (derived from the serpentinization of olivine) together with bastite pseudomorphs (serpentinized pyroxene) with minor small isolated veins of chrysotile and polygonal serpentine (Viti & Mellini, 1998). Mesh textures are formed by rims and cores: lizardite sectors constitute the rims and chaotic mixtures of lizardite and fibrous serpentines fill the cores (Figure 2b). Lizardite rims are typically up to ~150-μm thick and constituted by individual crystals up to ~3 μm, whereas core materials is constituted by ultrafine (<1 μm crystal size) associations of serpentines with random orientation (Figure 2b inset). Chaotic mixtures of lizardite, fibrous, and poorly crystalline serpentines, analogous to those in mesh core, constitute the bastites (Figure 2a inset). The edges of mesh texture, at the rim-rim boundaries, are often decorated with small magnetite grains that represent the residue of olivine serpentinization (e.g., Figure 1b).

The highly crystalline lizardite consists of large (up to mm size) euhedral crystals that form pseudohexagonal prisms with unusual elongation along [001] axis that corresponds to direction of vein openining (Figures 2c and S2). Lizardite (001) planes are therefore roughly perpendicular to the opening direction of the vein, with

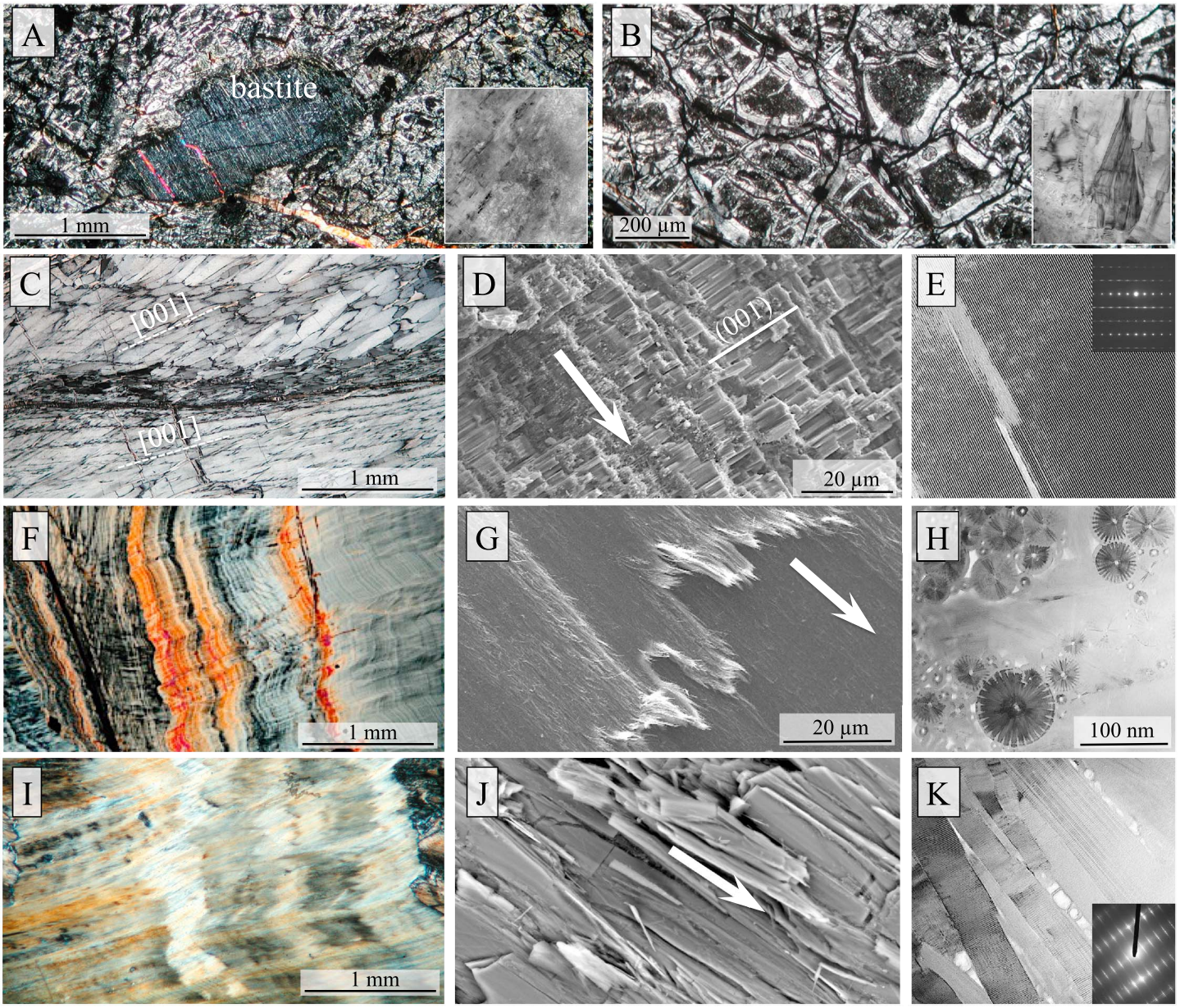

Figure 2. Characterization of serpentinite and serpentine minerals used in friction experiments. (a) Crossed nichols optical microscope image of retrograde serpentinite, with bastite (dark gray lamellar pseudomorph), mesh texture (white and black matrix) and chrysotile veinlets (high birefringence). Inset: transmission electron microscopy (TEM) image of the typical nanoscale mixture of lizardite, chrysotile and polygonal serpentine in bastites. Width: 1 µm. (b) Mesh texture deriving from olivine serpentinization: and consisting of light gray lizardite rims and dark cores of mixed serpentines. Inset: TEM image of lizardite sectors in mesh rims. Width 1 µm. (c) Large iso-oriented crystals of lizardite, crystal elongation (dashed line) corresponds to [001] axis and is parallel to the local opening direction (crossed nicols OM, section perpendicular to a shear plane). (d) Scanning electron microscopy (SEM) detail of lizardite crystals, with evident (001) cleavage planes. These planes are oriented perpendicular to the opening direction of the vein (arrow). (e) TEM detail of a lizardite crystal with regularly spaced 7 Å (001) planes. (f) Cross section of a slickenfiber vein constituted by fibrous serpentines (chrysotile and polygonal serpentine). (g) Secondary electron SEM image of fibrous serpentine slickenfiber isoriented with the slip direction of the fault (arrow). (h) TEM cross-section of fibrous serpentines: small chrysotile fibers (diameter $<$ 50 nm) mixed with large polygonal serpentine fibers (d ~ 100 nm) with radial sectors of planar (lizardite-like) serpentine layers. (i) Cross section of an antigorite "splintery" slickenfiber vein. (j) Secondary scanning electron microscopy image of antigorite lamellae isoriented in the shear direction (arrow). TEM image of tightly packed antigorite crystals with rare isolated chrysotile fibers. Inset: SAED pattern of antigorite.

rotational disorder around [001] (Figures 2d and 2e, and S3). Locally, small interstial spaces among closely packed lizardite crystals are occupied by isolated chrysotile fibers.

The reference sample for fibrous serpentines is represented by pale green slickenfibers composed of an ultra-fine association of chrysotile and polygonal serpentine fibers (Figures 2f and S4). Fiber bundles are mostly

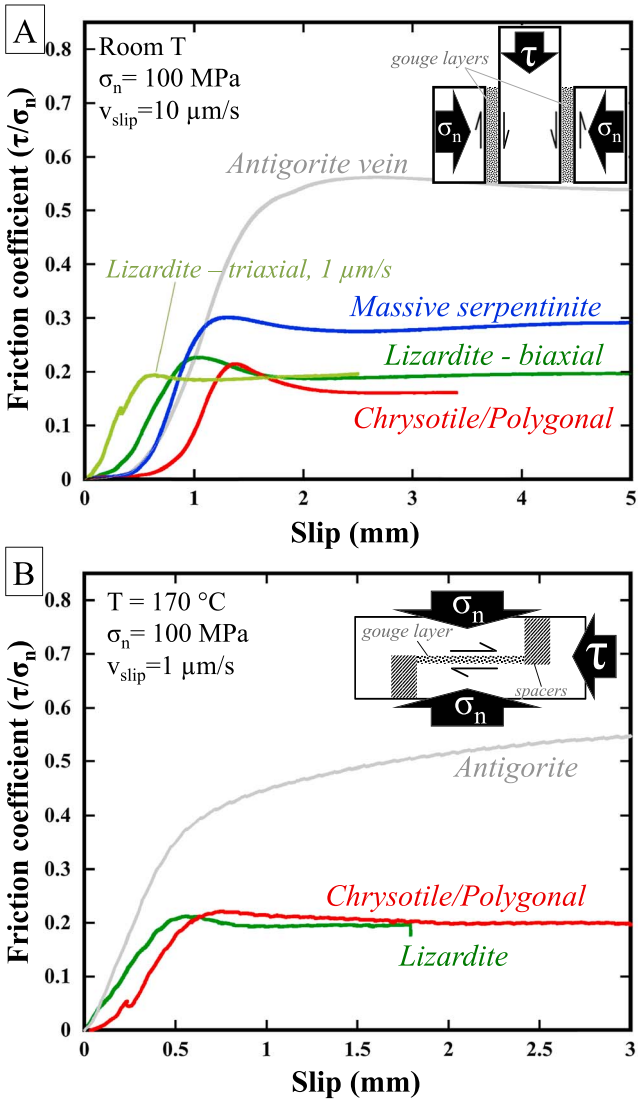

Figure 3. Examples of experimental friction curves. (a) Room temperature experiments on gouges antigorite (exp. i463, gray curve), massive serpentinites (experiment i386, blue), lizardite (experiment i289, dark green), and fibrous serpentines (chrysotile and polygonal serpentine, exp. i327, red) performed with the biaxial apparatus at normal stress σ_n = 100 MPa and sliding velocity v = 10 μm/s. Light green curve represents experiment Du85 carried out with the triaxial apparatus at room temperature, σ_n = 100 MPa and sliding velocity v = 1 μm/s on the same lizardite gouges. Inset: double direct shear geometry used in experiments with biaxial apparatus. (b) Examples friction curves in experiments carried out with the triaxial apparatus at T = 170°C, σ_n = 100 MPa and sliding velocity v = 1 μm/s on veins of lizardite (experiment Du89, green), fibrous serpentine (experiment Du90, red) and antigorite (experiment Du87, gray). Inset: single direct shear geometry used in experiments with the triaxial apparatus.

elongated in the shear direction (Figure 2g). Chrysotile fibers have cross-sectional diameter 30–40 nm and polygonal serpentine fibers are up to 500-nm thick (Figure 2h).

Pure antigorite was isolated form pale green splintery veins (Figures 2i and S7). These samples include antigorite lamellae up to tens of microns in size and with (010) planes oriented parallel to the shear direction of the slickenfiber (Figure 2j). TEM investigation revealed rare, isolated chrysotile fibers in the interstitial space (Figure 2k). Based on high resolution images and Selected Area Electron Diffraction (SAED) measurements (e.g., Figure 1k inset), average antigorite superstructure periodicity is 48.8 Å.

Finally, we selected a sample of prograde (thermometamorphic) antigorite serpentinite characterized by massive structure in the hand sample and mostly composed of antigorite (Figure S8). Antigorite in this sample is characterized by interpenetrating/interlocking texture ("bladed mat" texture, Maltman, 1978) due to static crystal growth, with average crystal size from a ~5–10 μm to a few hundreds of micrometers (Figure S8). Crystals of secondary olivine, with grain size ~50–10 μm and mostly derived by antigorite decomposition, are dispersed throughout the sample and represent ~15% of the sample volume.

3. Friction Experiments and Microstructural Observations

3.1. Experimental Methods

Friction experiments were performed using simulated fault gouges derived from our mineralogically controlled samples. The gouges were produced by separately crushing each sample in a disk mill, followed by sieving to obtain the fraction with grain size <250 μm. The same gouges were used to perform friction experiments at room and high temperature.

We performed room-temperature (~25°C) friction experiments in a servo-controlled biaxial deformation apparatus in the High Pressures-High Temperatures Laboratory of the Istituto Nazion ale di Geofisica e Vulcanologia in Rome, Italy (Collettini et al., 2014). We used a "double-direct" shear configuration in which two identical layers of sample are sandwiched between an assembly of three grooved steel blocks (Figure 3a inset, see also supporting information). The assembly was subject to the desired normal load applied perpendicular to the layers via the horizontal ram. and then sample layers were simultaneously sheared by driving the central block downward at constant or variable velocity, via the vertical ram (Figure 3a). The sliding area is maintained constant throughout the experiment (25 cm^2). With the exception of experiments i489 and i490, we imposed a sliding velocity of v = 10 μm/s during all biaxial experiments.

Friction tests at elevated temperature (T ~ 170°C, Figure 3b) were systematically performed on lizardite and fibrous serpentine gouges, which were previously observed to show a strength increase with temperatures above 100 ° C (Moore et al., 1997, 2004). One high temperature test was also performed on powders of antigorite veins to ensure the consistency of experimental results (Figure 3b). We used a direct-shear assembly within the triaxial vessel with fluid flow (DUTFF) equipped with an external furnace, hosted at the Rock Mechanics Laboratory of Durham University in Durham, UK (supporting information Figure S6). In this experimental configuration, a 8-cm^2 (initial value) layer of gouge is sandwiched between two L-shaped half-cylindrical pistons, offset using silicon rubber spacers (Figure 4b inset, see supporting information for complete description). The complete assembly is

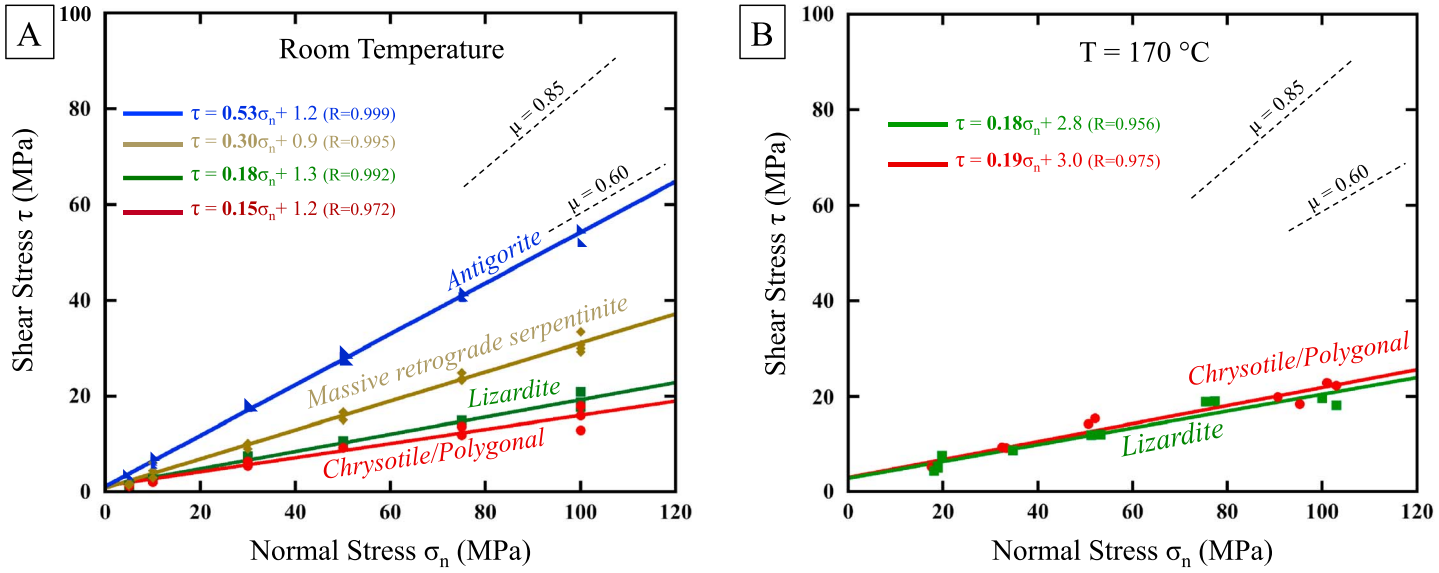

Figure 4. Coulomb failure envelopes of serpentine samples tested in this study. Shear stress was measured during steady state sliding phase within each friction experiment. The slope of the linear best fit represent the average coefficient of friction and the *y* intercept represents the cohesion. Typical friction of crustal rocks is shown for comparison (dashed lines, Byerlee, 1978). (a) Envelopes derived from room temperature experiments on antigorite (blue), massive retrograde serpentinite (brown), and fault-related veins lizardite (green) and chrysotile/polygonal serpentine (fibrous serpentines, red). The results of antigorite gouges represent both vein and massive samples together (see text for further explanation). (b) Envelopes for experiments carried out at T = 170°C on lizardite (green) and chrysotile/polygonal serpentine (fibrous serpentines, red) samples.

wrapped in a Teflon sheet and a Viton jacket and then is vertically inserted inside the vessel. The assembly/jacket strength is considered to be less than 0.1 kN (Leclère et al., 2016) and is considered negligible in the present study. In this configuration, the confining pressure of the vessel provides the normal stress and lateral confinement to the gouge. Shear stress and sliding was imposed to the gouge by the advancement of the axial piston, which was kept at the constant rate of 1 μm/s. In all DUTFF experiments, except Du85, the temperature was held constant at T ~ 170°C, to study the effect of temperature on the strength of serpentine gouges in comparison with room temperature tests.

We used optical microscopy and scanning electron microscopy (SEM) to examine deformation microstructures and to investigate links between mechanical data and the structural evolution of the sample. SEM analysis has been carried out using a Philips XL30 microscope, operating at 20 kV and equipped with an EDAX-DX4 energy dispersive spectrometer. SEM images were obtained from carbon-coated polished sections.

Table 1 lists all the experiments, materials, and experimental conditions of tests presented in this study.

3.2. Results

Figure 3 shows typical experimental results, with friction plotted as a function of displacement for serpentine samples. Friction presented in Figure 3 is computed as $\mu = \tau/\sigma_n$, that is, the ratio of shear stress τ and normal stress σ_n and shows the evolution of sample strength with increasing displacement. Following elastic loading, a slip hardening phase is observed as the sample begins to slide at the beginning of the experiment. After slip hardening, friction curves generally evolve with a rollover trend toward steady state values. We note that the slip hardening and rollover phases are progressively shorter at higher stress, for all tested materials (Figure S11). The rollover shown by the friction curves is thus interpreted as the mechanical manifestation of the initial reorientation of serpentine lamellae and fibers in addition to slip localization processes within the gouge. Samples of massive retrograde serpentinite, lizardite, and fibrous serpentines are frictionally weak with respect to typical values for crustal rocks ($\mu > 0.6$ Byerlee, 1978) and with respect to antigorite samples, either massive or veins ($\mu = 0.53$, Figure 3).

Massive retrograde serpentinite gouges ($\mu = 0.3$) are stronger than lizardite and fibrous serpentines, which show similarly low coefficients of friction ($\mu < 0.2$). In addition, Figure 3 shows that friction is not significantly affected by differences in temperature, slip velocity, and the type of experimental apparatus used in the tests, given the same composition and under the same normal stress. Moreover, we highlight that frictional weakness of

Table 1
List of Experiments, Sample Materials, and Experimental Conditions of Friction Experiments Presented in This Study

Experiment name	Material	Normal stress (MPa)	Sliding velocity[a]	Temperature
i287	Lizardite	10-30	10 μm/s	Room
i288	Lizardite	50-75	10 μm/s	Room
i289	Lizardite	100	10 μm/s	Room
i353	Lizardite	30-5-100	10 μm/s	Room
i489	Lizardite	100	1 μm/s	Room
i325	Chrysotile+Polygonal	50-75	10 μm/s	Room
i326	Chrysotile+Polygonal	10-30	10 μm/s	Room
i340	Chrysotile+Polygonal	50-75-30	10 μm/s	Room
i345	Chrysotile+Polygonal	30-5-100	10 μm/s	Room
i327	Chrysotile+Polygonal	100	10 μm/s	Room
i414	Chrysotile+Polygonal	30	10 μm/s	Room
i490	Chrysotile+Polygonal	100	1 μm/s	Room
i383	Massive retrograde serpentinite	5-50-75	10 μm/s	Room
i384	Massive retrograde serpentinite	10-30	10 μm/s	Room
i386	Massive retrograde serpentinite	100	10 μm/s	Room
i479	Massive retrograde serpentinite	100-50	10 μm/s	Room
i482	Massive retrograde serpentinite	75-30-10	10 μm/s	Room
i460	Antigorite (prograde serpentinite)	100	10 μm/s	Room
i461	Antigorite (prograde serpentinite)	50-75-10	10 μm/s	Room
i462	Antigorite (prograde serpentinite)	50-3010-5	10 μm/s	Room
i483	Antigorite (vein)	100-30-12	10 μm/s	Room
i480	Antigorite (vein)	100-75-50	10 μm/s	Room
i463	Antigorite (vein)	100	10 μm/s	Room
i464	Antigorite (vein)	75-50-30-25	10 μm/s	Room
Du87	Antigorite (vein)	100	1 μm/s	170°C
Du85	Lizardite	100	1 μm/s	Room
Du89	Lizardite	100[b]	1 μm/s	170°C
Du91	Lizardite	75-50[b]	1 μm/s	170°C
Du106	Lizardite	15[b]	1 μm/s	170°C
Du112	Lizardite	35-75[b]	1 μm/s	170°C
Du86	Chrysotile+Polygonal	100-75[b]	1 μm/s	170°C
Du92	Chrysotile+Polygonal	90[b]	1 μm/s	170°C
Du94	Chrysotile+Polygonal	50-30[b]	1 μm/s	170°C
Du90	Chrysotile+Polygonal	100-75[b]	1 μm/s	170°C
Du110	Chrysotile+Polygonal	15-30[b]	1 μm/s	170°C

[a]Load point velocity during steady state sliding. [b]Indicates the effective confining pressure (confining pressure – fluid pressure) within the triaxial vessel, equivalent to the normal stress on the sample, at the beginning of steady state sliding. Confining pressure increased during sliding in the triaxial vessel (see supporting information for details).

retrograde serpentines is not an artifact of our experimental setup, since antigorite gouges show a coefficient of friction similar to that measured in previous studies (e.g., Takahashi et al., 2011), at all tested conditions.

For each material, we determined a failure envelope that follows the Coulomb criterion:

$$\tau = \mu\sigma_n + c$$

where μ is the coefficient of friction, τ is the shear stress, measured during steady state sliding at constant imposed effective normal stress (σ_n), and c is the cohesion (Figure 4). The Coulomb criterion was computed by linear regression of the shear stress values measured during steady state sliding at different normal stress conditions. We consider the steady state shear stress to be representative of incipient slip on a fault rock with a localized microstructure, discarding the initial peak shear stress because it is the result of the random orientation of the gouge grains and heterogeneity of the deforming samples during the initial stage of shearing, before shear localization (see supporting information, Figure S11). Then, μ defines the normal stress dependence (and therefore depth dependence) of shear strength in the experimental faults. At room temperature, gouges obtained from prograde antigorite serpentinites and antigorite veins show identical failure envelopes (Figure S14). Therefore we produced a single failure envelope for antigorite combining data from all massive and vein samples (Figure 4a).

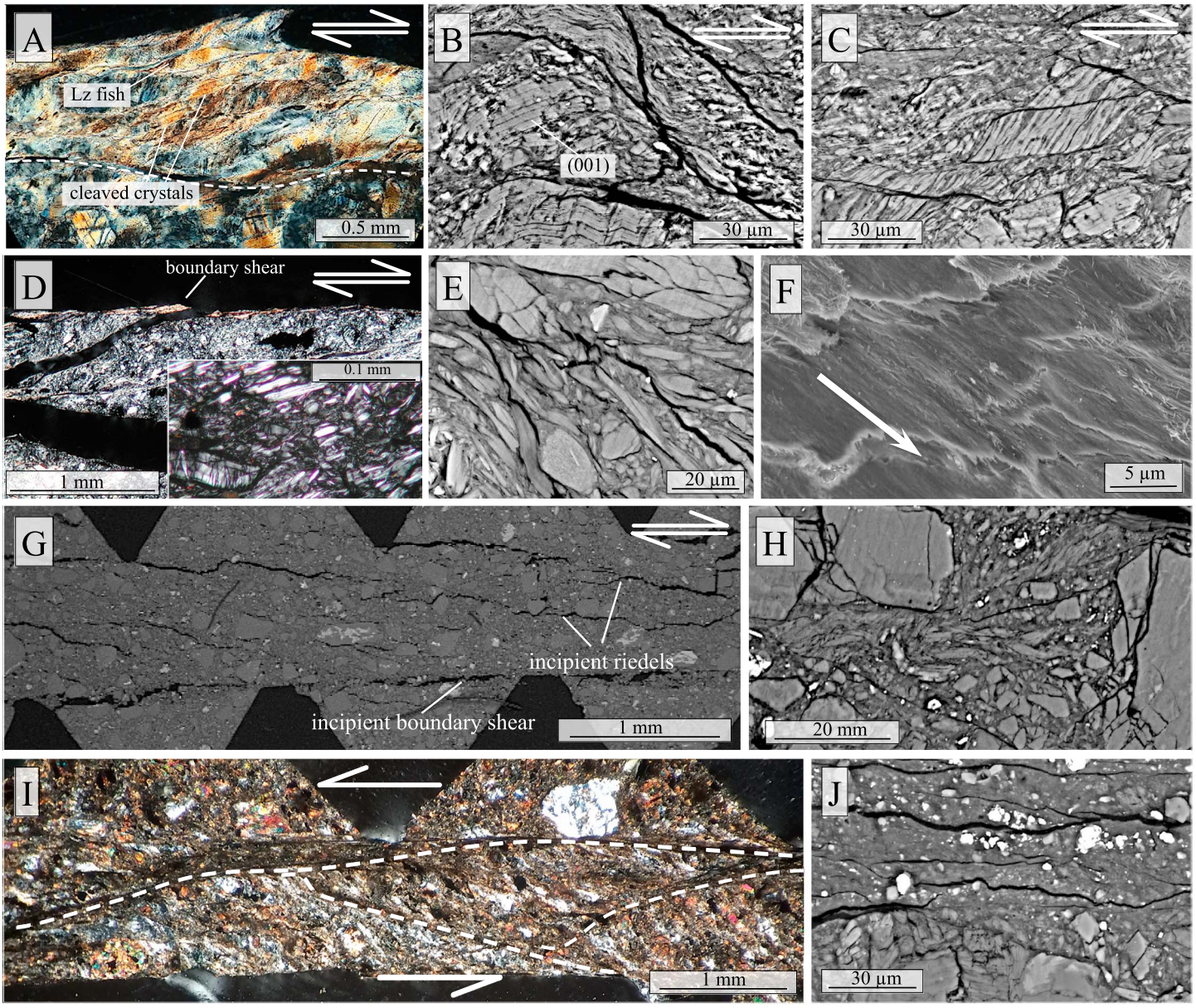

Figure 5. Posexperimental microstructures. (a) Structure of a boundary shear, delimited by a dashed line) in lizardite gouges (crossed Nichols, experiment i489). The boundary shear is intensely foliated, characterized by sigmoidal domains with ondulous extinction. Individual lizardite grains are cleaved along (001). (b) Scanning electron microscopy (SEM)-back scattered electron (BSE) detail of i489 gouge showing distributed flow accompanied by crystal delamination and folding. (c) SEM-BSE detail of a boundary shear in lizardite i489 showing folding and shearing with S/C(-C′) geometry. (d) Gouges of fibrous serpentine (experiment i325) with a thin localized boundary shear (high birefringence). Inset: pervasive iso-orientation of gouge clasts in less deformed parts of exp. i327. (e) SEM-BSE zoom within the bulk gouge (outside localization bands), showing imbrication of clasts and anastomosing fractures (left-lateral shear sense, experiment i325). (f) SEM-secondary electron detail of the boundary shear of experiment Du98 (fibrous serpentines) showing juxtaposed layers of iso-oriented chrysotile fibers. White arrow indicates the direction of slip. (g) SEM-BSE image of experiment i383 on massive retrograde serpentinite showing distributed grain size reduction in the whole sample thickness. Note that black areas are the trace of the grooves in the sample holder that prevent slip at the metal-gouge interface. Fracturing of the sample suggest the formation of incipient Riedels and boundary shears. (h) SEM-BSE detail of massive serpentinite gouge close to a Riedel fracture: Distributed cataclasis is the dominant deformation mode, accompanied by folding and delamination in limited portions of the matrix. (i) Deformed antigorite gouges (experiment i461) showing anastomosing shear bands (highlighted by dashed lines) characterized by grain size reduction and widespread foliation in the bulk of the gouge. (j) SEM-BSE detail of a boundary shear in antigorite gouges (experiment i460) showing cataclastic deformation in both serpentine (gray material) and secondary olivine (white grains).

In room temperature experiments, antigorite gouges are characterized by a high coefficient of friction $\mu = 0.53$, whereas all other gouges are frictionally weak, with $0.15 < \mu < 0.30$ (Figure 4a). Friction of massive retrograde serpentinites, whose mineralogy is dominated by lizardite and fibrous serpentines, is $\mu = 0.30$. Notably, veins of fibrous serpentines and lizardite, obtained from fault zones, have a lower frictional strength than undeformed massive serpentinite with same mineralogical composition (Figure 4a). In fact, at room temperature, chrysotile and polygonal serpentine mixtures (fibrous serpentines) show a low strength, $\mu = 0.15$. Similarly, gouges of lizardite exhibit $\mu = 0.18$ (Figure 4a). At room temperature, the cohesion is remarkably similar for all serpentine varieties, including antigorite, $c \sim 1$ MPa, represented by the intercept of the linear fit of each envelope (Figure 4a).

Experiments carried out in the heated triaxial vessel on chrysotile/polygonal serpentine and lizardite gouges reveal that the friction coefficient of these minerals is not significantly affected by temperature up to $T \sim 170$°C. Lizardite and fibrous serpentines remain weak showing $\mu = 0.19$ and $\mu = 0.18$, respectively (Figure 4b). At the same time, an appreciable increase in cohesion is observed with temperature to $c \sim 3$ MPa (Figure 4b).

3.3. Microstructural Observations

Postexperimental microstructures (Figure 5) of all samples show grain size reduction with respect to the starting gouge material but differ to each other in the degree of slip localization, intensity of comminution and deformation mechanisms.

Gouges of end-member serpentines, that is, antigorite, lizardite, and fibrous serpentines all show evidence of localized faulting along anastomosing Riedel, *P*, and boundary shears (Figures 5a–5f and 5i and 5j). Conversely, the deformation of massive retrograde serpentinites is more distributed throughout the thickness of the experimental sample, with only incipient Riedel and boundary shears (Figure 5g).

In gouges of lizardite (Figures 5a–5c) and fibrous serpentines (Figures 5d–5f), we observe intense foliations due to the alignment of platy grains that developed both in localized shear bands and in the adjacent, less deformed, gouge. In boundary shears of lizardite, these foliations are characterized by macroscopic S/C-C′ geometries and macroscopic "fish" of lizardite lamellae (Figure 5a and c). Individual S/C domains in the boundary shears present undulose extinction under crossed nicols, indicative of deformation in the crystal lattices. Individual large crystals of lizardite are delaminated within the boundary shear, with (001) basal planes parallel to the local slip direction (Figures 5a and 5b). Using the SEM, the crystal delamination along (001) planes is associated with microscale flow of finer particles by crystal folding (Figure 5b) and frictional slip that form S/CC′ geometries (Figure 5c). Comminution and slip in lizardite is therefore mostly accommodated by delamination by frictional sliding and/or dislocation glide along basal (001) planes.

Chrysotile and polygonal serpentine show widespread preferred orientation of fibers and gouge clasts across most of the sample thickness (Figure 5d inset) and the occurrence of very thin boundary shears (Figure 5d). At the microscale, the boundary shears are constituted by fine associations of dense microfibers that have abundant folding and anastomosed fractures (Figure 5e). Secondary electron SEM images reveal that the main boundary shears are constituted by several juxtaposed layers of fibrous serpentines (Figure 5f). In these layers, serpentine fibers are strongly iso-oriented along the slip direction, with a texture similar to that observed in natural slickenfibers (Figure 2g). Both features suggest frictional sliding and folding between fiber bundles during deformation.

Massive serpentinites show weak evidence for slip localization, and a relatively distributed grain size reduction, with the formation of only incipient Riedel and boundary shears (Figure 5g). Deformation of these gouges occurs predominantly by cataclasis, producing heterogeneous angular clasts, in particular close to incipient Riedels (Figure 5h). Magnetite and other minor phases appear to be distributed throughout the sample but not interconnected, thus scarcely affecting the deformation microstructures (e.g., Figures 5g and 5h). Within small zones of finer grain size, we observe deformation microstructures similar to those observed in pure lizardite and fibrous serpentine gouges (local preferred orientation, folding, delamination and fibers alignment, Figure 5h). However, the presence of intact mesh textures within large grains and slightly higher frictional strength suggests that at least macroscopically, delamination of lizardite crystals is not an efficient deformation mechanism in gouges of massive serpentinite (see below).

The deformation of antigorite (Figures 5i and 5j) is characterized by localization along narrow and curved Riedels and boundary shears that experience intense grain size reduction. Outside these bands of slip

localization, the gouge shows a diffuse *P* foliation of the gouge (Figure 5i). SEM investigation reveals that grain size reduction in localized shear bands occur by cataclastic processes that produce angular grains and abundant intragranular and intergranular, predominantly mode I, fractures (Figure 5j). Olivine grains that are present only in gouges from massive prograde antigorite serpentinite (e.g., Figure 5j) show cataclastic grain size reduction and are distributed in shear bands (e.g., Figure S19).

4. Discussion

4.1. The Role of Serpentine Mineralogy and Rock Fabric on Frictional Strength

In discussing our mechanical data and their implications for the strength of brittle faults, we emphasize that friction is measured at slow sliding velocities (1–100 μm/s), and therefore, it can be considered as a proxy for the "static" fault strength during the interseismic periods or during preseismic phases. Dynamic weakening mechanisms of serpentinites occurring at high slip velocities (e.g., Hirose & Bystricky, 2007; Proctor et al., 2014) are not considered in our analysis.

The Coulomb failure envelopes are strongly linear for all studied samples (τ versus σ_n fits have $0.952 < R < 0.999$, Figure 4) highlighting that deformation can be consistently described as "brittle" and that different friction values emerge from different contributions of dilatancy during shear, that is, work against the confining pressure.

Our experiments highlight a marked strength difference between antigorite gouges and all retrograde serpentines, either massive serpentinites or veins of lizardite and fibrous serpentines. Antigorite gouges at room temperature show relatively high strength, $\mu = 0.53$, which is consistent with previous friction experiment on this mineral that have shown friction $0.50 < \mu < 0.75$ in the temperature range 25–600°C and at low pressures (e.g., Moore et al., 1996, 1997; Reinen et al., 1994; Takahashi et al., 2011). At low *P-T*, high strength is the result of cataclastic deformation in localized bands (Figures 5g and 5h), which correlates well with the crystallographic structure of antigorite. In the antigorite structure, strong interlayer bonds promote relatively high fracture (and frictional) strength and favor fracturing with respect to frictional sliding along the basal planes. Fracturing is the fundamental deformation process also beyond the laboratory brittle-ductile transition. At higher confining pressures, that is, $P_c > 250$ MPa, antigorite deform by distributed cataclastic flow (Escartin et al., 1997) that is substituted by dislocation glide only at elevated pressures >1 GPa (Amiguet et al., 2014). The predominance of fracturing over sliding on the basal planes also explains the identical strength and deformation mechanisms we document for samples of massive prograde serpentinites and antigorite veins that are characterized by interpenetrating, interlocked crystals, and iso-oriented lamellae, respectively.

Conversely, gouges derived from massive retrograde serpentinite, constituted mostly by lizardite with significant amounts of fibrous serpentines, are frictionally weak, $\mu = 0.30$. Pure samples of lizardite and fibrous serpentines are even weaker, $0.15 < \mu < 0.19$, and this weakness is maintained in the temperature range of 25–170°C. In the following, we first focus on the general weakness of lizardite and fibrous serpentines, and then we discuss why friction of gouge derived from veins is lower than that of gouges from massive serpentinites that have similar mineralogical composition.

The microstructural evidence of crystal delamination in lizardite, and slip along fiber bundles in fibrous serpentine strongly suggests that frictional sliding and dislocation glide are the active deformation processes at all tested experimental conditions. Sliding along phyllosilicate lamellae and/or along fibers can be assimilated to mode II or III fractures, which imply less dilatant opening during shear deformation with respect to cataclastic deformation, which is dominated by dilatant mode I and wing cracks. Minor dilatation during shear implies less work against the confining pressure/normal stress, resulting in the macroscopic frictional weakness of lizardite and fibrous serpentines (Figures 3 and 4). Preferential mode II failure along (001) planes was previously suggested to explain the weakness of intact cores of antigorite- and lizardite-dominated serpentinites, at relatively high confining stress ($P >$ ~200 MPa; Escartin et al., 1997). Here we show evidence that mode II fracturing, frictional sliding and dislocation glide along serpentine lamellae and fibers, can also be active deformation mechanisms at much lower pressures ($P < 150$ MPa) in simulated fault gouges.

In lizardite crystals, successive layers are weakly bonded to one another by hydrogen bonds that favor interlayer delamination (e.g., Evans, 2004). In chrysotile, the concentric arrangement of (001) planes do not favor crystal delamination; however, individual fibers are loosely bound by van der Waals interaction and therefore

frictional sliding between fibers is favored. Polygonal serpentine, which is constituted by concentric sectors of lizardite-like platy serpentine, may experience a combination of internal deformation by basal gliding and interfiber slip mechanisms.

However, both mechanisms are likely to occur in tandem with other processes during brittle shearing of retrograde serpentines. More specifically, slip interlocking of adjacent gouge grains with different spatial orientations and, in the case of fibrous serpentine gouges, tangling of mineral fibers are likely to limit the efficiency of basal frictional slip/gliding and interfiber slip. These misorientations can cause folding and fracturing of crystals, which are clearly observed in deformed serpentines (e.g., Figures 5c–5h, see also Amiguet et al., 2012; Hirauchi & Katayama, 2013).

The friction of massive retrograde serpentinites is higher than that of lizardite and fibrous serpentines (Figure 4a), in spite of their similar mineralogical composition. Massive serpentinite grains of the experimental gouges derive from mesh textures and bastites of the original rock, where the serpentine crystals have very small size and are randomly oriented at the scale of the whole rock (Figures 2a and 2b). In addition, the presence of magnetite grains in these samples may contribute to increase the friction, even though they are dispersed throughout the gouge and are unlikely to have a significant effect on the serpentinite strength. With respect to pure lizardite gouges that are constituted by large and isoriented crystals (particle size $<$250 μm), the clasts in the gouge form massive serpentinites maintain the random structure and fine grain size of the original rock. This intrinsic fabric of the rock is preserved inside the gouge clasts and likely results in a higher degree of slip interlocking. This has to be accommodated through grain fracturing and folding of crystals, reducing the efficiency of nondilatant deformation of lizardite and fibrous serpentines, thus yielding slightly higher shear strength. This is consistent with the microstructure and deformation mechanisms observed in gouges of retrograde serpentinites (e.g., distributed cataclasis and only incipient brittle localization in Figures 5g and 5h) that are very different compared to those observed in pure lizardite gouges (Figures 5c–5e).

The presence of pure, large, and iso-oriented crystal size in our lizardite gouges could also explain the lower frictional strength, μ = 0.18, and lower data dispersion obtained in our experiments, compared to that of lizardite reported in previous studies (i.e., μ = 0.30–0.56, Figure 1). From the available information in previous studies, gouges used to measure the strength of lizardite were mostly derived from massive serpentinites (e.g., Moore et al., 1996, 1997; Moore & Lockner, 2011; Raleigh & Paterson, 1965; Rutter & Brodie, 1988). Then it is possible to infer that these rocks were probably similar to our samples of retrograde serpentinties and thus characterized by relatively fine crystal size, mesh textures, and the presence of variable amounts (up to ~15–20% in volume) of accessory phases that are stronger than pure retrograde serpentines, such as magnetite, brucite, and chlorite (μ ~ 0.3–0.4, Ikari et al., 2009; Morrow et al., 2000), spinel, and olivine (μ ~ 0.5–0.7, Raleigh & Paterson, 1965). We suggest that the random structure of the original rocks used to produce the gouge may have resulted in a limited efficiency of nondilatant processes, similarly to what we document in gouges of massive retrograde serpentinites. In addition, the variable secondary phases present in massive retrograde serpentinites may have contributed to indicate higher and scattered values of friction for lizardite (e.g., Figure 1). Unfortunately, these hypotheses remain mostly untested because of the scarcity of microstructural evidence about the deformation processes of lizardite gouges in experiments conducted at conditions similar to those presented in this study (but see, e.g., "cataclastic" lizardite gouges in Moore & Lockner, 2011).

Additional differences with previous studies may derive from different experimental techniques such as the use of saw-cut geometries instead of direct shear geometries or the use of different jacketing materials in the sample assembly. For instance, the use of finer grain sizes in tested gouges, reported in previous studies to be smaller than 90 μm (e.g., Behnsen & Faulkner, 2012; Moore et al., 1997; Reinen et al., 1994), may reduce the proportion of grain contacts along (001) (e.g., Behnsen & Faulkner, 2012), therefore reducing the efficiency of slip along basal planes and making the crystal folding more difficult. The influence of these factors on the results of friction experiments are, however, difficult to assess and should be an area of future investigation.

From the results of our friction tests we suggest that strain localisation along almost pure and iso-oriented slickenfibers results in a dramatic weakening of fault rocks, with a strength reduction up to ~50% with respect to their massive counterparts with randomly oriented crystals.

4.2. Implications for the Strength of Serpentine-Rich Faults

In this section, we discuss the implications of our experiments for the strength of serpentine-bearing fault zones in the brittle and seismogenic lithosphere. In the field, the typical mesoscale structure of retrograde serpentine-bearing fault zones is characterized by anastomosing schistosity and brittle faults wrapping around blocks of massive serpentinite (e.g., Figure S1, Andréani et al., 2005; Hirauchi & Yamaguchi, 2007; Keller & Pialli, 1990; Maltman, 1978; Twiss & Gefell, 1990). These faults are typically wholly coated with serpentine slickenfibers sometimes accompanied by cataclasites and gouge, indicating a predominantly brittle (dilatant) mode of deformation (e.g., Hoogerdujin Strating & Vissers, 1994; Twiss & Gefell, 1990) accompanied by dissolution-crystallization processes, often without dynamic recrystallization (Andréani et al., 2005, 2007; Bellot, 2008; Hirauchi & Yamaguchi, 2007). Consistently with this fault structure, massive serpentinites can be considered as the intact host rocks (protolith) of slickenfibers and gouges, which in turn represent the main brittle fault rocks in serpentine-bearing shear zones. The above observations then validate the use of friction experiments and, in particular, the use of serpentine gouges obtained from coatings of natural slip surfaces (i.e., the vein/slickenfiber samples) to investigate the strength of these faults.

At *P-T* conditions comparable to our experiments, lizardite, and fibrous serpentines (chrysotile and polygonal serpentine) are the dominant minerals in retrograde serpentine-bearing fault zones. Conversely, antigorite is the stable serpentine variety at elevated temperature conditions, $T > 300$–350°C (Evans, 2004). Then our results on antigorite friction, albeit consistent with previous literature, have been obtained at low-temperature conditions and thus are relevant mostly for faulting and reactivation in deeply exhumed serpentinitic bodies. Under the conditions of the uppermost crust, the strength of antigorite-filled faults is not significantly different from the strength of other common rocks (e.g., Byerlee, 1978) and will not be discussed further in the present study.

Conversely, lizardite and fibrous serpentines (chrysotile and polygonal serpentine) are important minerals in major fault zones. In the following we briefly review the occurrence of fault-related hydration of ultramafic rocks with crystallization of lizardite and fibrous serpentines.

Retrograde serpentinites have been extensively dredged and cored along walls of major transform faults in the oceans (e.g., Bonatti, 1968, 1978; Mével, 2003, and references therein) and crop out on exhumed transforms (e.g., Bailey et al., 2000; Irwin & Barnes, 1975). Abundant serpentinized peridotites are recovered from slow- and ultraslow-spreading oceanic ridges, typically associated to detachment faulting (e.g., Karson et al., 2006; Mével, 2003; Sauter et al., 2013) and, rarely, in faults at fast-spreading ridges (e.g., Früh-Green et al., 1996). Serpentines may not be ubiquitous in oceanic detachments, which typically intersect extremely heterogeneous lithosphere and in which abundant talc-rich and amphibolitic fault rocks (e.g., Boschi et al., 2006; Escartín et al., 2003, for an extensive review, Miranda & Dilek, 2010), ophicalcites (e.g., Manatschal & Müntener, 2009) or even silicified breccias (Karson et al., 2006) are found. However, many of these rocks may be interpreted as matasomatic alteration products of preexisting serpentinites or due to incorporation of heterogeneous materials along complex fault zones during the exhumation of serpentinized upper mantle (e.g., Bonnemains et al., 2017; Karson et al., 2006).

Lizardite and fibrous serpentines are also considered the main constituents of altered mantle rocks below rifted, hyperextended continental margins and at the ocean-continent transition (Beslier et al., 1996; Boillot et al., 1980; Bonatti & Michael, 1989; Reston & McDermott, 2011). Along these magma-starved rifted margins, subcontinental mantle is hydrated by faults cutting the crust and unroofed by long-lived detachments localized at the crust-mantle boundary, which may be regarded as precursors, and kinematically analogue, of detachments at mid-ocean ridges (e.g., Floyd et al., 2001; Reston, 1990; Reston & McDermott, 2011). Lizardite and fibrous serpentines, commonly associated to minor chlorite and talc also constitute the main rock-forming minerals in the walls and fault rocks of subcontinental or oceanic detachments that have been recognized in exhumed fault zones (e.g., Manatschal et al., 2011; Manatschal & Müntener, 2009).

Moreover, reduced seismic velocities and elevated V_p/V_s ratios in the lower crust and upper mantle of subducting plates suggest that a significant degree of low-temperature serpentinization may occur along large normal faults induced by slab bending (e.g., Grevemeyer et al., 2018; Ranero et al., 2003). Finally, serpentines are extensively recognized and studied in faults of ophiolitic units (e.g., Dilek, 2003, and references therein, Hoogerdujin Strating & Vissers, 1994; Twiss & Gefell, 1990).

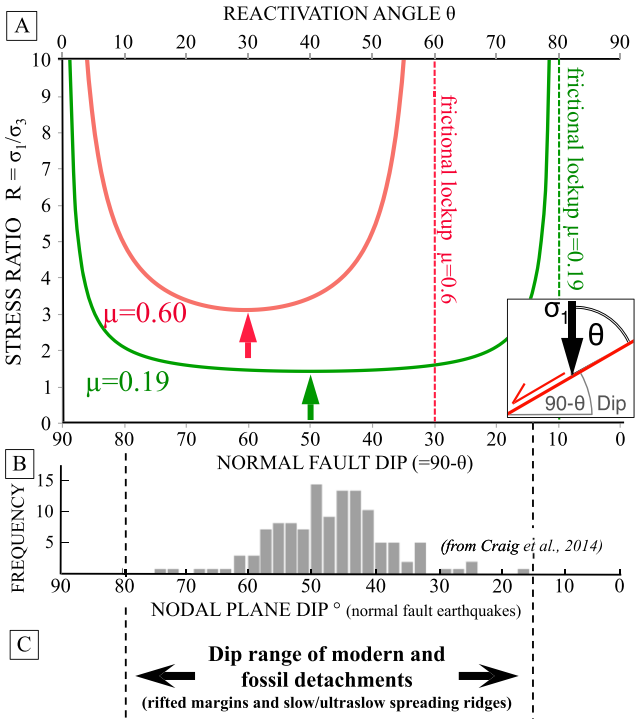

Figure 6. (a) Stress ratio *R* versus reactivation angle (top) versus normal fault dip (bottom) for "strong" faults (μ = 0.6, red) and weak serpentine-bearing faults (μ = 0.19, green). The arrows indicate the *R* minimum and the optimum reactivation angles for strong and weak faults, respectively. Inset: in an extensional environment characterized by vertical σ_1 trajectories, the reactivation angle, θ, is complementary to the fault dip. (b) Reactivation angle is compared to the dip distribution of focal mechanisms of earthquakes occurring along normal faults from several oceanic outer rises (redrawn from Craig et al., 2014). Seismicity clustering in the 60°–40° dip range correspond to favorable orientations predicted by the reactivation criterion for μ = 0.19 (green curve minima). (c) Dip range of activity of modern and fossil detachments at slow/ultraslow spreading ridges and magma-poor rifted margins (references and explanation in the text).

The results of friction experiments then suggest that all these major faults should be predominantly weak, with effective coefficients of friction $\mu < 0.2$, provided that retrograde serpentines represent the main constituents of the fault rocks (see above). It is worth to emphasize that in natural fault zones, further weakening is caused by the concomitant action of dissolution-precipitation processes (e.g., Fagereng, 2013; Tesei et al., 2015; Wallis et al., 2015), which likely promote frictional-viscous flow (e.g., Niemeijer & Spiers, 2007). As a consequence, the frictional strength we determine in the laboratory is a measure of relatively fast brittle deformation processes and likely represents only an upper bound to the strength of natural serpentine-bearing faults.

4.3. Frictional Fault Reactivation Analysis

To address the question of how our mechanical data apply to serpentine-bearing faults, we compared the mechanical prediction of our frictional measurements presented Figure 4 with (1) the dip distribution of active normal faults at oceanic outer rises, obtained from earthquake data and (2) the dip range of modern and fossil detachments at rifted margins and slow spreading ridges (Figure 6).

To investigate the influence of weak serpentines on the conditions for fault activity, we computed the stress ratio *R* necessary for fault reactivation, for a two-dimensional case. Considering an existing fault containing the intermediate principal stress axis and lying at an angle θ to the maximum compressive stress (Figure 5 inset), the stress ratio is defined as

$$R = \sigma_1/\sigma_3 = (1 + \mu \cot\theta)/(1-\mu \tan\theta)$$

where σ_1 and σ_3 are the maximum and minimum effective principal stresses, respectively, μ is the coefficient of friction along the fault and θ is the reactivation angle (Sibson, 1985). The optimal condition for fault reactivation is given by the minimum of *R* and its associated optimum reactivation angle, θ_{opt}. Away from this optimal value, the stress ratio increases as faults becomes increasingly misoriented for reactivation. *R* tends to infinity when θ approaches the frictional lock-up angle. Beyond the frictional lockup angle, the formation of a new fault is favored over the reactivation of a severely misorientated fault (Sibson, 1985).

Following this, we computed the stress ratio *R* obtained for weak serpentines (lizardite and fibrous serpentine) using the maximum friction values we measured, that is, μ = 0.19 (Figure 6a, green curve), as a conservative estimate to evaluate the potential for fault reactivation. We compare these values with *R* computed for strong faults, μ = 0.6 (Figure 6a, red curve). Our experimental data predict that weak serpentine-bearing faults have an optimal reactivation angle of θ_{opt} = 40° and a frictional lockup at $\theta \approx 80°$, whereas strong faults have an optimal reactivation angle of θ_{opt} = 30° and a frictional lockup at $\theta \approx 60°$.

Moreover, with respect to strong faults, frictionally weak faults need much lower absolute values of *R*, and hence lower differential stress, to be reactivated across a wider range of θ (Figure 6a). For instance, Figure 6 highlights that within a given stress field with $R \sim 3$, only well-oriented strong faults with θ around 30° are reactivated. Conversely, all serpentine-bearing faults, lying at $\theta = 5° - 75°$ to the maximum compressive stress, can be potentially reactivated for nearly the same stress ratio.

These mechanical predictions can be tested against the dip distribution of earthquake nodal planes at the outer rise of subduction zones, where extensive serpentinization occurs (e.g., Grevemeyer et al., 2018, and references therein). Normal fault earthquakes occurring in the outer rise are characterized by fault dips clustering around 45° ± 5 (Craig et al., 2014, Figure 6b), very close to the optimal reactivation angle obtained for weak serpentine-rich faults, when friction obtained from our experiments is implied (Figure 6a). Moreover, we note that the low friction of serpentines can also explain several events on

faults dipping less than 40°, which would otherwise be misoriented or severely misoriented if typical Byerlee friction coefficients are assumed.

Further evidence supporting the weakness of serpentine-rich faults comes from the geometry of active and fossil detachments observed at rifted margins and slow/ultraslow spreading mid-ocean ridges (Figure 6c). Detachments at mid-ocean ridges potentially initiate as high-angle structures beneath the ridge axis, with dips ~70° ± 10° (deMartin et al., 2007; MacLeod et al., 2009; Tucholke et al., 1998). During their lifecycle, these faults flatten out, rotating to low angles due to flexural unloading of the footwall ("rolling hinge model," Buck, 1988), until they are eventually abandoned and dissected by later normal faults (e.g., Sauter et al., 2013; Smith et al., 2006). The angle of emergence from the seafloor and the cross-cutting relationships of detachments with late faults may suggest that detachments, at and away from the ridge axis, were active and able to accommodate lithospheric extension until their dip was ~10–20° (e.g., Cannat et al., 2009). Their counterparts on magma-poor rifted continental margins show similar kinematic histories, with ductile, high-angle roots, and low-angle detachment faulting unroofing mantle rocks (e.g., Reston & McDermott, 2011). Synrift sediments deposited on top of these detachments constrain that in several cases, subcontintental detachments were active at dips $<$35° and, perhaps, as low as 15°–10° (e.g., Floyd et al., 2001; Reston et al., 2007).

In summary, modern and fossil detachments at both rifted margins and slow/ultraslow mid-ocean ridges show fault dips in the approximate range 15°–80°, during active slip (Figure 6c). Remarkably, these dip range coincide with those predicted by fault reactivation theory based on our friction results (Figure 6c). Low measured friction values of lizardite and fibrous serpentines (μ = 0.15–0.19) allow sliding of extensional detachments at dips as low as ~10° (frictional lockup of serpentine, Figure 6a).

Thus, we suggest that our constraints on friction for lizardite and fibrous serpentines provide, together with their metasomatic alteration such as talc (e.g., Boschi et al., 2006; Moore & Rymer, 2007), a simple mechanical explanation for the efficiency of detachment faulting in accommodating crustal extension.

5. Conclusions

We document the frictional properties of a suite of serpentine samples for which the mineralogy was thoroughly assessed from the hand sample down to the nanoscale. We studied the friction of serpentine samples from fault surfaces representing the main end-members of the serpentine varieties: antigorite, lizardite, and fibrous serpentine (chrysotile and polygonal serpentine) and massive samples of serpentinites. Antigorite has a relatively high coefficient of friction, μ = 0.53, whereas all other samples are frictionally weak, $\mu \leq 0.3$. Slickenfibers of lizardite, chrysotile, and polygonal serpentine are significantly weaker ($\mu < 0.2$) than their massive counterpart (μ = 0.3), notwithstanding their similar mineralogy. We conclude that the highly oriented microstructures of slickenfibers, attained along faults, promote a highly efficient nondilatant deformation resulting in low friction. The low friction of lizardite and fibrous serpentine varieties is maintained up to relatively elevated temperatures ($T < 200$°C), suggesting the inherent weakness of serpentine-bearing faults in the uppermost seismogenic lithosphere.

Finally, integrating friction data with predictions from fault reactivation analysis, our data provide a simple mechanical explanation for independent geological and geophysical observations about the weakness of major serpentine-bearing faults.

Acknowledgments
This research was funded by the European Commission with the Marie Sklodowska-Curie Fellowship STRAIN (748400) to T. T., the ERC Starting Grant GLASS (259256) to CC, and by a NERC CASE studentship grant EP/M507854/1 to C. W. A. H. Data presented in Figure 4 are publicly available at https://www.researchgate.net/profile/Telemaco_Tesei. We thank Matt Ikari and an anonymous reviewer, who helped improve the present manuscript.

References

Amiguet, E., Reynard, B., Caracas, R., Van de Moortèle, B., Hilairet, N., & Wang, Y. (2012). Creep of phyllosilicates at the onset of plate tectonics. *Earth and Planetary Science Letters*, *345*, 142–150.

Amiguet, E., Van De Moortèle, B., Cordier, P., Hilairet, N., & Reynard, B. (2014). Deformation mechanisms and rheology of serpentines in experiments and in nature. *Journal of Geophysical Research: Solid Earth*, *119*, 4640–4655. https://doi.org/10.1002/2013JB010791

Andréani, M., Boullier, A. M., & Gratier, J. P. (2005). Development of schistosity by dissolution–crystallization in a Californian serpentinite gouge. *Journal of Structural Geology*, *27*(12), 2256–2267. https://doi.org/10.1016/j.jsg.2005.08.004

Andréani, M., Mével, C., Boullier, A. M., & Escartin, J. (2007). Dynamic control on serpentine crystallization in veins: Constraints on hydration processes in oceanic peridotites. *Geochemistry, Geophysics, Geosystems*, *8*, Q02012. https://doi.org/10.1029/2006GC001373

Bailey, W. R., Holdsworth, R. E., & Swarbrick, R. E. (2000). Kinematic history of a reactivated oceanic suture: The Mamonia complex suture zone, SW Cyprus. *Journal of the Geological Society*, *157*(6), 1107–1126. https://doi.org/10.1144/jgs.157.6.1107

Behnsen, J., & Faulkner, D. R. (2012). The effect of mineralogy and effective normal stress on frictional strength of sheet silicates. *Journal of Structural Geology*, *42*, 49–61. https://doi.org/10.1016/j.jsg.2012.06.015

Bellot, J. P. (2008). Natural deformation related to serpentinisation of an ultramafic inclusion within a continental shear zone: The key role of fluids. *Tectonophysics*, *449*(1–4), 133–144. https://doi.org/10.1016/j.tecto.2007.11.054

Beslier, M.O., Cornen, G., & Girardeau, J. (1996). Tectono-metamorphic evolution of peridotites from the ocean/continent transition of the Iberia Abyssal lain margin. In *Proceedings - Ocean Drilling Program scientific results* (pp. 397-412). National Science Foundation.

Boillot, G., Grimaud, S., Mauffret, A., Mougenot, D., Kornprobst, J., Mergoil-Daniel, J., & Torrent, G. (1980). Ocean-continent boundary off the Iberian margin: A serpentinite diapir west of the Galicia Bank. *Earth and Planetary Science Letters*, *48*(1), 23–34. https://doi.org/10.1016/0012-821X(80)90166-1

Bonatti, E. (1968). Ultramafic rocks from the mid-Atlantic ridge. *Nature*, *219*(5152), 363.

Bonatti, E. (1978). Vertical tectonism in oceanic fracture zones. *Earth and Planetary Science Letters*, *37*(3), 369–379. https://doi.org/10.1016/0012-821X(78)90052-3

Bonatti, E., & Michael, P. J. (1989). Mantle peridotites from continental rifts to ocean basins to subduction zones. *Earth and Planetary Science Letters*, *91*(3–4), 297–311. https://doi.org/10.1016/0012-821X(89)90005-8

Bonnemains, D., Escartín, J., Mével, C., Andreani, M., & Verlaguet, A. (2017). Pervasive silicification and hanging wall overplating along the 13°20′N oceanic detachment fault (Mid-Atlantic Ridge). *Geochemistry, Geophysics, Geosystems*, *18*, 2028–2053. https://doi.org/10.1002/2017GC006846

Bortolotti, V., Fazzuoli, M., Pandeli, E., Principi, G., Babbini, A., & Corti, S. (2007). Geology of central and eastern Elba Island, Italy. *Ofioliti*, *26*(2a), 97–150.

Boschi, C., Früh-Green, G. L., & Escartín, J. (2006). Occurrence and significance of serpentinite-hosted, talc-and amphibole-rich fault rocks in modern oceanic settings and ophiolite complexes: An overview. *Ofioliti*, *31*(2), 129–140.

Buck, W. R. (1988). Flexural rotation of normal faults. *Tectonics*, *7*, 959–973. https://doi.org/10.1029/TC007i005p00959

Byerlee, J. (1978). Friction of rocks. In *Rock friction and earthquake prediction* (pp. 615–626). Basel: Birkhäuser.

Cannat, M., Sauter, D., Escartín, J., Lavier, L., & Picazo, S. (2009). Oceanic corrugated surfaces and the strength of the axial lithosphere at slow spreading ridges. *Earth and Planetary Science Letters*, *288*(1–2), 174–183. https://doi.org/10.1016/j.epsl.2009.09.020

Coleman, R. G. (1971). Plate tectonic emplacement of upper mantle peridotites along continental edges. *Journal of Geophysical Research*, *76*, 1212–1222. https://doi.org/10.1029/JB076i005p01212

Collettini, C., Di Stefano, G., Carpenter, B., Scarlato, P., Tesei, T., Mollo, S., et al. (2014). A novel and versatile apparatus for brittle rock deformation. *International Journal of Rock Mechanics and Mining Sciences*, *66*, 114–123. https://doi.org/10.1016/j.ijrmms.2013.12.005

Craig, T. J., Copley, A., & Middleton, T. A. (2014). Constraining fault friction in oceanic lithosphere using the dip angles of newly-formed faults at outer rises. *Earth and Planetary Science Letters*, *392*, 94–99. https://doi.org/10.1016/j.epsl.2014.02.024

deMartin, B. J., Sohn, R. A., Canales, J. P., & Humphris, S. E. (2007). Kinematics and geometry of active detachment faulting beneath the Trans-Atlantic Geotraverse (TAG) hydrothermal field on the Mid-Atlantic Ridge. *Geology*, *35*(8), 711–714. https://doi.org/10.1130/G23718A.1

Dengo, C. A., & Logan, J. M. (1981). Implications of the mechanical and frictional behavior of serpentinite to seismogenic faulting. *Journal of Geophysical Research*, *86*(B11), 10,771–10,782.

Deschamps, F., Godard, M., Guillot, S., & Hattori, K. (2013). Geochemistry of subduction zone serpentinites: A review. *Lithos*, *178*, 96–127. https://doi.org/10.1016/j.lithos.2013.05.019

Dilek, Y. (2003). Ophiolite concept and its evolution. *Special Papers-Geological Society of America*, *373*, 1–16.

Escartin, J., Hirth, G., & Evans, B. (1997). Nondilatant brittle deformation of serpentinites: Implications for Mohr-coulomb theory and the strength of faults. *Journal of Geophysical Research*, *102*, 2897–2913. https://doi.org/10.1029/96JB02792

Escartin, J., Hirth, G., & Evans, B. (2001). Strength of slightly serpentinized peridotites: Implications for the tectonics of oceanic lithosphere. *Geology*, *29*(11), 1023–1026. https://doi.org/10.1130/0091-7613(2001)029%3C1023:SOSSPI%3E2.0.CO;2

Escartín, J., Mével, C., MacLeod, C. J., & McCaig, A. M. (2003). Constraints on deformation conditions and the origin of oceanic detachments: The mid-Atlantic ridge core complex at 15 45′ N. *Geochemistry, Geophysics, Geosystems*, *4*(8), 1067. https://doi.org/10.1029/2002GC000472

Evans, B. W. (2004). The serpentinite multisystem revisited: Chrysotile is metastable. *International Geology Review*, *46*(6), 479–506. https://doi.org/10.2747/0020-6814.46.6.479

Fagereng, Å. (2013). On stress and strain in a continuous-discontinuous shear zone undergoing simple shear and volume loss. *Journal of Structural Geology*, *50*, 44–53. https://doi.org/10.1016/j.jsg.2012.02.016

Floyd, J. S., Mutter, J. C., Goodliffe, A. M., & Taylor, B. (2001). Evidence for fault weakness and fluid flow within an active low-angle normal fault. *Nature*, *411*(6839), 779.

Früh-Green, G. L., Plas, A., & Lécuyer, C. (1996). 14. Petrologic and stable isotope constraints on hydrothermal alteration and serpentinization of the EPR shallow mantle at Hess deep (site 895). *Proceeding of the Ocean Drilling Program, Scientific Results*, *147*, 255–291.

Grevemeyer, I., Ranero, C. R., & Ivandic, M. (2018). Structure of oceanic crust and serpentinization at subduction trenches. *Geosphere*, *14*(2), 395–418.

Guillot, S., Schwartz, S., Reynard, B., Agard, P., & Prigent, C. (2015). Tectonic significance of serpentinites. *Tectonophysics*, *646*, 1–19. https://doi.org/10.1016/j.tecto.2015.01.020

Hirauchi, K. I., & Katayama, I. (2013). Rheological contrast between serpentine species and implications for slab–mantle wedge decoupling. *Tectonophysics*, *608*, 545–551. https://doi.org/10.1016/j.tecto.2013.08.027

Hirauchi, K. I., & Yamaguchi, H. (2007). Unique deformation processes involving the recrystallization of chrysotile within serpentinite: Implications for aseismic slip events within subduction zones. *Terra Nova*, *19*(6), 454–461. https://doi.org/10.1111/j.1365-3121.2007.00771.x

Hirose, T., & Bystricky, M. (2007). Extreme dynamic weakening of faults during dehydration by coseismic shear heating. *Geophysical Research Letters*, *34*, L14311. https://doi.org/10.1029/2007GL030049

Hoogerdujin Strating, E. H., & Vissers, R. L. (1994). Structures in natural serpentinite gouges. *Journal of Structural Geology*, *16*(9), 1205–1215. https://doi.org/10.1016/0191-8141(94)90064-7

Ikari, M. J., Saffer, D. M., & Marone, C. (2009). Frictional and hydrologic properties of clay-rich fault gouge. *Journal of Geophysical Research*, *114*, B05409. https://doi.org/10.1029/2008JB006089

Irwin, W. P., & Barnes, I. (1975). Effect of geologic structure and metamorphic fluids on seismic behavior of the San Andreas fault system in central and northern California. *Geology*, *3*(12), 713–716. https://doi.org/10.1130/0091-7613(1975)3%3C713:EOGSAM%3E2.0.CO;2

Karson, J. A., Früh-Green, G. L., Kelley, D. S., Williams, E. A., Yoerger, D. R., & Jakuba, M. (2006). Detachment shear zone of the Atlantis massif core complex, mid-Atlantic ridge, 30 N. *Geochemistry, Geophysics, Geosystems*, *7*, Q06016. https://doi.org/10.1029/2005GC001109

Keller, J. V. A., & Pialli, G. (1990). Tectonics of the Island of Elba; a reappraisal. *Bollettino della Societa Geologica Italiana*, *109*(2), 413–425.

Leclère, H., Faulkner, D., Wheeler, J., & Mariani, E. (2016). Permeability control on transient slip weakening during gypsum dehydration: Implications for earthquakes in subduction zones. *Earth and Planetary Science Letters*, *442*, 1–12. https://doi.org/10.1016/j.epsl.2016.02.015

MacLeod, C. J., Searle, R. C., Murton, B. J., Casey, J. F., Mallows, C., Unsworth, S. C., et al. (2009). Life cycle of oceanic core complexes. *Earth and Planetary Science Letters*, *287*(3-4), 333–344. https://doi.org/10.1016/j.epsl.2009.08.016

Maltman, A. J. (1978). Serpentinite textures in Anglesey, North Wales, United Kingdom. *Geological Society of America Bulletin*, *89*(7), 972–980. https://doi.org/10.1130/0016-7606(1978)89%3C972:STIANW%3E2.0.CO;2

Manatschal, G., & Müntener, O. (2009). A type sequence across an ancient magma-poor ocean–continent transition: The example of the western alpine Tethys ophiolites. *Tectonophysics*, *473*(1–2), 4–19. https://doi.org/10.1016/j.tecto.2008.07.021

Manatschal, G., Sauter, D., Karpoff, A. M., Masini, E., Mohn, G., & Lagabrielle, Y. (2011). The Chenaillet ophiolite in the French/Italian alps: An ancient analogue for an oceanic core complex? *Lithos*, *124*(3–4), 169–184. https://doi.org/10.1016/j.lithos.2010.10.017

Mellini, M., & Viti, C. (1994). Crystal structure of lizardite-1T from Elba, Italy. *American Mineralogist*, *79*(11–12), 1194–1198.

Mével, C. (2003). Serpentinization of abyssal peridotites at mid-ocean ridges. *Comptes Rendus Geoscience*, *335*(10–11), 825–852. https://doi.org/10.1016/j.crte.2003.08.006

Miranda, E. A., & Dilek, Y. (2010). Oceanic core complex development in modern and ancient oceanic lithosphere: Gabbro-localized versus peridotite-localized detachment models. *The Journal of Geology*, *118*(1), 95–109.

Moore, D. E., & Lockner, D. A. (2011). Frictional strengths of talc-serpentine and talc-quartz mixtures. *Journal of Geophysical Research*, *116*, B01403. https://doi.org/10.1029/2010JB007881

Moore, D. E., Lockner, D. A., Ma, S., Summers, R., & Byerlee, J. D. (1997). Strengths of serpentinite gouges at elevated temperatures. *Journal of Geophysical Research*, *102*, 14,787–14,801. https://doi.org/10.1029/97JB00995

Moore, D. E., Lockner, D. A., Summers, R., Byerlee, J. D., & Ma, S. (1996). Sample characterizations and strength measurements of serpentinite gouges. *U.S. Geological Survey Open-File Report*, 96–702.

Moore, D. E., Lockner, D. A., Tanaka, H., & Iwata, K. (2004). The coefficient of friction of chrysotile gouge at seismogenic depths. *International Geology Review*, *46*(5), 385–398. https://doi.org/10.2747/0020-6814.46.5.385

Moore, D. E., & Rymer, M. J. (2007). Talc-bearing serpentinite and the creeping section of the San Andreas fault. *Nature*, *448*(7155), 795.

Morrow, C. A., Moore, D. E., & Lockner, D. A. (2000). The effect of mineral bond strength and adsorbed water on fault gouge frictional strength. *Geophysical Research Letters*, *27*, 815–818. https://doi.org/10.1029/1999GL008401

Niemeijer, A. R., & Spiers, C. J. (2007). A microphysical model for strong velocity weakening in phyllosilicate-bearing fault gouges. *Journal of Geophysical Research*, *112*, 10405. https://doi.org/10.1029/2007JB005008

Proctor, B. P., Mitchell, T. M., Hirth, G., Goldsby, D., Zorzi, F., Platt, J. D., & Di Toro, G. (2014). Dynamic weakening of serpentinite gouges and bare surfaces at seismic slip rates. *Journal of Geophysical Research: Solid Earth*, *119*, 8107–8131. https://doi.org/10.1002/2014JB011057

Raleigh, C. B., & Paterson, M. S. (1965). Experimental deformation of serpentinite and its tectonic implications. *Journal of Geophysical Research*, *70*, 3965–3985. https://doi.org/10.1029/JZ070i016p03965

Ranero, C. R., Morgan, J. P., McIntosh, K., & Reichert, C. (2003). Bending-related faulting and mantle serpentinization at the Middle America trench. *Nature*, *425*(6956), 367.

Reinen, L. A., Weeks, J. D., & Tullis, T. E. (1994). The frictional behavior of lizardite and antigorite serpentinites: Experiments, constitutive models, and implications for natural faults. *Pure and Applied Geophysics*, *143*(1–3), 317–358. https://doi.org/10.1007/BF00874334

Reston, T. J. (1990). Mantle shear zones and the evolution of the northern North Sea basin. *Geology*, *18*(3), 272–275.

Reston, T. J., Leythäuser, T., Booth-Rea, G., Sawyer, D., Klaeschen, D., & Long, C. (2007). Movement along a low-angle normal fault: The S reflector west of Spain. *Geochemistry, Geophysics, Geosystems*, *8*, Q06002. https://doi.org/10.1029/2006GC001437

Reston, T. J., & McDermott, K. G. (2011). Successive detachment faults and mantle unroofing at magma-poor rifted margins. *Geology*, *39*(11), 1071–1074. https://doi.org/10.1130/G32428.1

Rutter, E. H., & Brodie, K. (1988). Experimental "syntectonic" dehydration of serpentinite under conditions of controlled pore water pressure. *Journal of Geophysical Research*, *93*, 4907–4932. https://doi.org/10.1029/JB093iB05p04907

Sauter, D., Cannat, M., Rouméjon, S., Andreani, M., Birot, D., Bronner, A., et al. (2013). Continuous exhumation of mantle-derived rocks at the Southwest Indian Ridge for 11 million years. *Nature Geoscience*, *6*(4), 314.

Schwartz, S., Guillot, S., Reynard, B., Lafay, R., Debret, B., Nicollet, C., et al. (2013). Pressure–temperature estimates of the lizardite/antigorite transition in high pressure serpentinites. *Lithos*, *178*, 197–210. https://doi.org/10.1016/j.lithos.2012.11.023

Sibson, R. H. (1985). A note on fault reactivation. *Journal of Structural Geology*, *7*(6), 751–754. https://doi.org/10.1016/0191-8141(85)90150-6

Smith, D. K., Cann, J. R., & Escartín, J. (2006). Widespread active detachment faulting and core complex formation near 13 N on the Mid-Atlantic Ridge. *Nature*, *442*(7101), 440.

Summers, R., & Byerlee, J. (1977). A note on the effect of fault gouge composition on the stability of frictional sliding. In *International Journal of Rock Mechanics and Mining Sciences & Geomechanics Abstracts* (Vol. 14, No. 3, pp. 155–160). Pergamon.

Takahashi, M., Uehara, S. I., Mizoguchi, K., Shimizu, I., Okazaki, K., & Masuda, K. (2011). On the transient response of serpentine (antigorite) gouge to stepwise changes in slip velocity under high-temperature conditions. *Journal of Geophysical Research*, *116*, B10405. https://doi.org/10.1029/2010JB008062

Tesei, T., Lacroix, B., & Collettini, C. (2015). Fault strength in thin-skinned tectonic wedges across the smectite-illite transition: Constraints from friction experiments and critical tapers. *Geology*, *43*(10), 923–926. https://doi.org/10.1130/G36978.1

Tucholke, B. E., Lin, J., & Kleinrock, M. C. (1998). Megamullions and mullion structure defining oceanic metamorphic core complexes on the mid-Atlantic ridge. *Journal of Geophysical Research*, *103*, 9857–9866. https://doi.org/10.1029/98JB00167

Twiss, R. J., & Gefell, M. J. (1990). Curved slickenfibers: A new brittle shear sense indicator with application to a sheared serpentinite. *Journal of Structural Geology*, *12*(4), 471–481. https://doi.org/10.1016/0191-8141(90)90035-W

Viti, C., & Hirose, T. (2010). Thermal decomposition of serpentine during coseismic faulting: Nanostructures and mineral reactions. *Journal of Structural Geology*, *32*(10), 1476–1484. https://doi.org/10.1016/j.jsg.2010.09.009

Viti, C., & Mellini, M. (1996). Vein antigorites from Elba Island, Italy. *European Journal of Mineralogy*, *8*(2), 423–434. https://doi.org/10.1127/ejm/8/2/0423

Viti, C., & Mellini, M. (1998). Mesh textures and bastites in the Elba retrograde serpentinites. *European Journal of Mineralogy*, *10*(6), 1341–1360. https://doi.org/10.1127/ejm/10/6/1341

Wallis, D., Lloyd, G. E., Phillips, R. J., Parsons, A. J., & Walshaw, R. D. (2015). Low effective fault strength due to frictional-viscous flow in phyllonites, Karakoram fault zone, NW India. *Journal of Structural Geology*, *77*, 45–61. https://doi.org/10.1016/j.jsg.2015.05.010

Wicks, F. J., & Whittaker, E. J. W. (1977). Serpentine textures and serpentinization. *Canadian Mineralogist*, *15*(4), 459–488.